PHOTONICS Research

Integrating the optical tweezers and spanner onto an individual single-layer metasurface

Tianyue Li,[1] Xiaohao Xu,[2,4] Boyan Fu,[1] Shuming Wang,[1,3,5] Baojun Li,[2] Zhenlin Wang,[1] and Shining Zhu[1,3]

[1]National Laboratory of Solid-State Microstructures, School of Physics, College of Engineering and Applied Sciences, Nanjing University, Nanjing 210093, China
[2]Institute of Nanophotonics, Jinan University, Guangzhou 511443, China
[3]Key Laboratory of Intelligent Optical Sensing and Manipulation, Ministry of Education, Nanjing 210093, China
[4]e-mail: xuxhao@jnu.edu.cn
[5]e-mail: wangshuming@nju.edu.cn

Received 28 January 2021; revised 1 April 2021; accepted 1 April 2021; posted 2 April 2021 (Doc. ID 421121); published 25 May 2021

Optical tweezers (OTs) and optical spanners (OSs) are powerful tools of optical manipulation, which are responsible for particle trapping and rotation, respectively. Conventionally, the OT and OS are built using bulky three-dimensional devices, such as microscope objectives and spatial light modulators. Recently, metasurfaces are proposed for setting up them on a microscale platform, which greatly miniaturizes the systems. However, the realization of both OT and OS with one identical metasurface is posing a challenge. Here, we offer a metasurface-based solution to integrate the OT and OS. Using the prevailing approach based on geometric and dynamic phases, we show that it is possible to construct an output field, which promises a high-numerical-aperture focal spot, accompanied with a coaxial vortex. Optical trapping and rotation are numerically demonstrated by estimating the mechanical effects on a particle probe. Moreover, we demonstrate an on-demand control of the OT-to-OS distance and the topological charge possessed by the OS. By revealing the OT–OS metasurfaces, our results may empower advanced applications in on-chip particle manipulation.

https://doi.org/10.1364/PRJ.421121

1. INTRODUCTION

Optical tweezers (OTs), consisting of a tightly focused beam [1], give a contactless way to trap and accurately position small particles. Such ability is attributed to the intensity gradient in the focused field, which induces a restoring force for confining the particles in three dimensions (3D) [2–5]. Nowadays, the OT has become a widely valuable tool in many fields, especially in biophysics [6], and it also provides a typical platform for conducting rigorous and specific phenomena in both classical and quantum light–matter interactions [7–12]. On the other hand, when carrying angular momentum, light can exert torques on the particles, driving them to rotate continuously [13–16]. The tool capable of particle rotation is known as the optical spanner (OS) [17–21], comprising a donut shape with a helical wave-front, and it gives an additional degree of freedom for manipulating objects. In fact, while the OS is most known for its ability in rotating particles, it can also be used to trap particles when the intensity gradient force is repulsive [22,23].

The manipulation of particles with light requires a careful shaping of light itself, and since the OT and OS are based on dramatically different fields, they generally rely on distinct devices for wave-front modulation. To achieve the aforementioned functions with stable trapping and durable spanning, traditionally the beam in the OT is focused by high-numerical-aperture (NA) objectives into a diffraction-limited spot [1,2], while the vortex beam in the OS is usually generated with spatial light modulators [14]. Nevertheless, these relatively bulky devices make it difficult to integrate the OT and OS together, especially in small systems, such as optical fiber and optofluidic platforms.

During the last decade, metasurfaces composed of an array of subwavelength nanostructures have exhibited exceptional strength in the full control over the polarization, amplitude, and phase of light [24–27], and the tremendous booming of applications in nanoscale has been reported [28–33]. A conventional metasurface is primarily dependent on either the geometric phase (i.e., Pancharatnam–Berry phase) or the dynamic phase by means of rotating the orientation angle relative to the reference axis of meta-atoms and the geometry of several specific nanostructures, separately [24,26,27]. Instead, the latest works have revealed that the syntheses of two types of these phases possess the superiority of multiplexing two functionalities into a single metasurface [33–37], which offers an unprecedented opportunity to set up OT and OS with a compact and

miniaturized device. Up to now, while the metasurface-based OT or OS has been severally implemented through unitary light field generation [38–43], a structure enabling both the OT and OS is yet to be reported. In this paper, we introduce a versatile metasurface, which integrates the functionality of both OT and OS onto an individual single-layer device. We realize this OT–OS metasurface by using the interplay of the geometric and the dynamic phases, by which the metasurface holds two independent optical responses. As a result, dual focal planes are yielded for the output field, and the focal lengths and topological charges can be tailored at will.

2. METASURFACE IMPLEMENTATION

Figure 1(a) schematically illustrates the OT–OS metasurface device, excited by a linearly polarized plane wave of wavelength $\lambda = 532$ nm. The output field is featured by sharp intensity gradient and helical phase structures, which are separated coaxially, capable of particle trapping and rotation, respectively. To see how the output field is produced, let us consider an optical element described by a Jones matrix $J(x,y)$ and normally illuminated by a plane wave (defined as the vector ket $|E_0\rangle$. When the light field passing through the element, the output field becomes $J(x,y)|E_0\rangle$. In this process, two independent phase profiles, ϕ_x and ϕ_y, can be generated in synergy with the polarization of incident field $|E_0\rangle$. Assuming that the polarization bases of interest are $|k^+\rangle$ and $|k^-\rangle$ with $\langle k^+|k^-\rangle = 0$, one may express the spatially varying Jones matrix $J(x,y)$ as

$$J(x,y) = e^{i\phi^+(x,y)}|(k^+)^*\rangle\langle k^+| + e^{i\phi^-(x,y)}|(k^-)^*\rangle\langle k^-|, \quad (1)$$

where * denotes the complex conjugate, and

$$|k^+\rangle = |L\rangle = \frac{1}{\sqrt{2}}\begin{bmatrix}1\\ i\end{bmatrix}, |k^-\rangle = |R\rangle = \frac{1}{\sqrt{2}}\begin{bmatrix}1\\ -i\end{bmatrix}, \quad (2)$$

represent left-handed circular polarization (LCP) and right-handed circular polarization (RCP). It follows that independent phase profiles determined by the orthogonally polarized bases can be superimposed on the same device. In other words, two optical responses are achieved by simultaneously allowing the orthogonal polarization states to satisfy different phase profiles. Therefore, the Jones matrix can be rewritten as

$$J(x,y) = \frac{1}{2}\begin{bmatrix} e^{i\phi^+(x,y)} & e^{i\phi^-(x,y)} \\ -ie^{i\phi^+(x,y)} & -ie^{i\phi^-(x,y)}\end{bmatrix}\begin{bmatrix}1 & 1\\ i & -i\end{bmatrix}^{-1}. \quad (3)$$

The unitary matrix of Eq. (3) can be diagonalized by solving the characteristic equation, and the basis of eigenvalues and eigenvectors of $J(x,y)$ can be obtained (See Appendix A). It is found that an anisotropic meta-atom can be considered as a birefringent waveguide [24] because of the high index contrast between the nanobrick and the air, while the phase shifts (ϕ_x, ϕ_y) along the two perpendicular symmetry axes and the specific orientation angle θ along the $x-y$ plane can satisfy the optical element Jones matrix $J(x,y)$. The calculated relation indicates that θ and the difference between the phase shifts, $\phi_x - \phi_y$, can be analytically expressed by

$$|\phi_x - \phi_y| = \pi, \quad (4)$$

and

$$\phi^+(x,y) - \phi^-(x,y) = 4\theta. \quad (5)$$

It is worth noting that Eq. (4) is attributed to the accumulations of the dynamic phase, which needs to build a phase library of nanobricks by varying the geometry of the nanobrick, while Eq. (5) is controlled only by the rotation of the orientation angle θ. Through the combination of the dynamic phase and the geometric phase, when the linear plane wave passes through a nanobrick, the LCP and RCP states can be transformed into their orthogonal polarization states and hold the same dynamic phase and opposite geometric phase to realize independent optical manipulation.

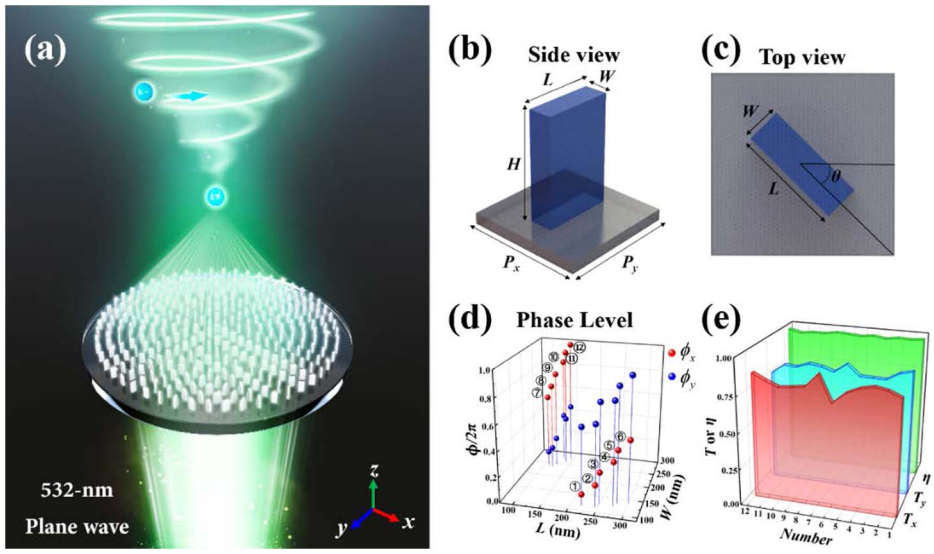

Fig. 1. (a) Schematic diagram of the polarization-dependent OT–OS metasurface. (b), (c) Typical unit cell of the OT–OS metasurface with period P_x, P_y, height H, varying width W, length L (side view), and rotation angle θ along the $x-y$ plane (top view). (d) Phase level of twelve labeled nanobricks, together with (e) corresponding transmittances and polarization conversion efficiencies of the selected nanofins.

3. OT–OS METASURFACE DEVICE REALIZATION

Based on the theory mentioned above, the specifically designed unit cell, composed of a fused SiO_2 substrate (refractive index: $n_{SiO_2} = 1.46$), on which TiO_2 ($n_{TiO_2} = 2.40$) nanobricks are periodically arranged with fixed lattice constant $P_x = P_y = 450$ nm and height $H = 600$ nm, is shown in Figs. 1(b) and 1(c). Finite-difference time domain (FDTD) simulations are performed to calculate transmittance by using the commercial software package "FDTD Solutions" (Lumerical Inc.). Periodic boundary conditions are applied along the x and y axes, and the perfectly matched layers (PMLs) are applied to the z direction. The range of lengths (L) and widths (W) of the nanofins covers 50 to 400 nm, for 5 nm increments of each geometric variable, and the results of continuous phase shifts ϕ_x and ϕ_y along the x and y axes are approximated into twelve discrete phase levels, high transmittances, and polarization conversion efficiencies, as shown in Figs. 1(d) and 1(e). The detailed parameters of each nanobrick can be found in Appendix B.

According to this discussion, the polarization-sensitive metasurface has two independent optical responses and, hence, holds the possibility for integrating the OT and OS. To implement this device, the focused phase formula must be introduced as follows:

$$\phi^{+}(x,y,f_{\mathrm{OT}}) = -2\pi\left(\sqrt{x^2+y^2+f_{\mathrm{OT}}^2} - f_{\mathrm{OT}}\right)/\lambda, \tag{6}$$

$$\phi^{-}(x,y,f_{\mathrm{OS}}) = -2\pi\left(\sqrt{x^2+y^2+f_{\mathrm{OS}}^2} - f_{\mathrm{OS}}\right)/\lambda + l\varphi, \tag{7}$$

where (x, y) denotes the coordinate of each nanobrick on the metasurface, and f_{OT} and f_{OS} are the focal lengths for each response. Also, an additional vortex term $l\varphi$ in Eq. (7) is required for the phase profile of the OS, where l denotes topological charge, and $\varphi = \arctan(y/x)$ represents the azimuthal angle.

Figure 2(a) illustrates the top, zoomed, and angled views of the metasuface configuration. The radius of the entire metasurface is $R = 8$ μm, and there are 918 nanobricks used in the full-metasurface design. Figure 2(b) shows the output field distribution, for a metasurface designed by setting $l = 1$ and two focal lengths, $f_{\mathrm{OT}} = 6.0$ μm and $f_{\mathrm{OS}} = 9.5$ μm. Two planes of local intensity maxima can be identified at $z = 6.0$ and 9.5 μm, in agreement with the theory. Specially, at $z = 6.0$ μm, the field is focused into a spot with a waist radius about 0.285 μm [Fig. 2(c)], corresponding to an NA of ~0.8. On the other hand, the field around $z = 9.5$ μm constructs the OS, characterized by ring-like intensity and helical phase distributions [Fig. 2(d)].

For a small particle that can be approximated as an electric dipole, its dynamic behavior in the optical field can be predicted by the dipole model, in which the j component ($j = x, y, z$) of the optical force is given by [3]

$$\langle \mathbf{F}_e \rangle_j = \frac{1}{2}\mathrm{Re}(\alpha E_k \partial_j E_k^*), \tag{8}$$

where α is the complex polarizability, and E_k is k component ($k = x, y, z$) of the incident field. Equation (8) can be decomposed into two parts:

$$\begin{aligned}\langle \mathbf{F}_e \rangle_j &= \langle \mathbf{F}_{\mathrm{Gra}} \rangle_j + \langle \mathbf{F}_{\mathrm{Rad}} \rangle_j \\ &= \frac{1}{4}\mathrm{Re}(\alpha)\partial_j|\mathbf{E}|^2 - \frac{1}{2}\mathrm{Im}(\alpha)\mathrm{Im}(E_k \partial_j E_k^*),\end{aligned} \tag{9}$$

where the first part is known as the intensity gradient force, and the second part is the radiation pressure. For $\mathrm{Re}(\alpha) > 0$ (which is true for dielectric nanoparticles), the gradient force will point to the intensity maximum. In this case, the OT tends to trap the particle around the focus center, while the OS is expected to confine it away from the beam axis.

To understand how the particle rotation can be achieved by the OS, one may write the complex electric field as

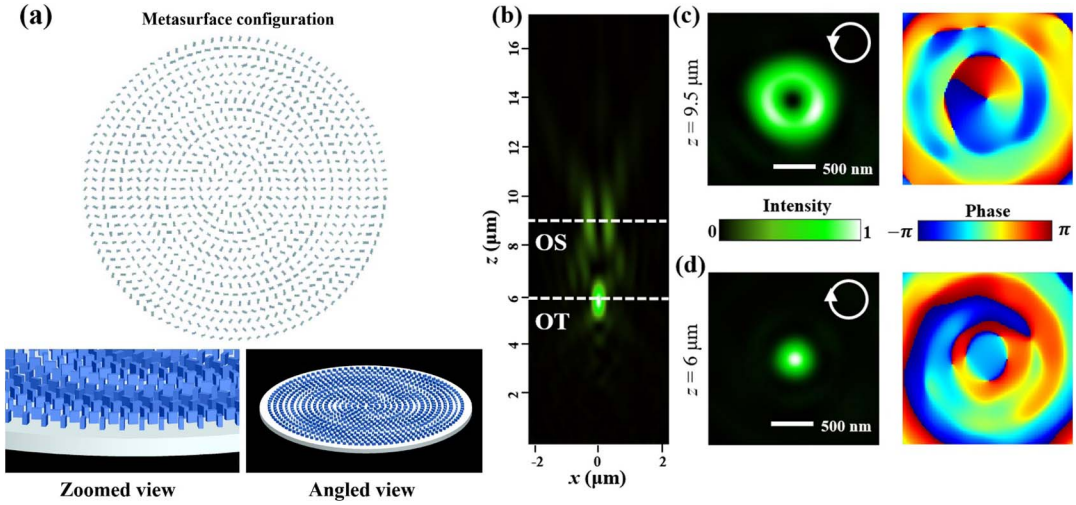

Fig. 2. Simulation for the OT–OS metasurface. (a) The entire OT–OS metasurface configuration with top, zoomed, and angled 3D perspective view. (b) Axial section view of the intensity distribution. The dashed lines indicate the focal plane for the function of OT and OS. (c), (d) Transverse section views of the intensity (left column) and phase (right column) distributions at the focal plane of the OS and OT, respectively. The phase profiles are responsible for the transverse fields. White arrows indicate the polarization state.

$E_k = E_{0k}\exp(i\Phi k)$, where E_{0k} and Φ_k represent the amplitude and phase, respectively. Then, the radiation pressure can be expressed as

$$\langle \mathbf{F}_{\mathrm{Rad}}\rangle_j = -\frac{1}{2}\mathrm{Im}(\alpha)\mathrm{Im}(E_k\partial_j E_k^*) = \frac{1}{2}\mathrm{Im}(\alpha)(E_{0k}^2\partial_j\Phi_k), \tag{10}$$

which is associated with the phase gradient of the field. Since the OS has a helical phase structure [see Fig. 2(c)], the phase gradient and, hence, the radiation pressure will acquire an azimuthal component, setting the particle into rotation about the beam axis.

To verify the manipulation ability of the OT–OS metasurface, numerical calculations were performed by using a polystyrene (PS) nanosphere (radius: $R_{\mathrm{PS}} = 100$ nm; $n_{\mathrm{PS}} = 1.59$) as a probe. The optical force is computed rigorously by Maxwell stress tensor method [15,44–46]:

$$\langle \mathbf{F}\rangle = \oint \langle \mathbf{T}_{\mathrm{M}}\rangle \cdot \mathbf{n}\mathrm{d}\sigma, \tag{11}$$

where $\mathbf{n}$ is the unit vector outward normally to the surface σ enclosing the particle, and $\langle \mathbf{T}_{\mathrm{M}}\rangle$ is the time-averaged Maxwell stress tensor. Note that Eq. (11) reduces to Eq. (8) for the electric dipolar approximation [15].

Figure 3 shows the calculated force exerted on the particle placed at different positions on the $y = 0$ plane. When the particle is close to the tight focusing spot, 3D trapping arises at $x = 0$ and $z = 6.5$ μm, as indicated by Figs. 3(a) and 3(b). The transverse and longitudinal trapping stiffnesses [47] are estimated to be $\kappa_x = 199.78\ \mathrm{pN}\cdot\mu\mathrm{m}^{-1}\cdot\mathrm{W}^{-1}$ and $\kappa_z = 19.38\ \mathrm{pN}\cdot\mu\mathrm{m}^{-1}\cdot\mathrm{W}^{-1}$, respectively. We also notice in Fig. 3(b) the appearance of a small y-component force when the particle deviates from the equilibrium position. This should be caused by Belinfante's spin current due to spin inhomogeneity [44,48–50]. By contrast, when the particle is located around the OS, the zero points of the x- and z-component forces occur around $x = -0.4$ μm and $z = 10.4$ μm, as shown by Figs. 3(c) and 3(d). However, at this position, F_y is shown to be nonzero, and the direction of the force agrees with the phase gradient indicated by Fig. 2(c). These indicate an off-axis trapping, along with an anticlockwise rotation of the particle about the optics axis.

4. DISCUSSION AND CONCLUSION

We have shown the simultaneous creation of the OT and OS, with a longitudinal separation distance of $\Delta f = 3.5$ μm and the topological charge of the OS being $l = 1$. Next, we shall explore the possibility of changing Δf and l. Since the polarization-dependent design principle provides a different phase profile with independent control, the focal length of the output field can be adjustable. Figure 4(a), as an example, demonstrates an enhanced OT-to-OS distance, $\Delta f = 6.0$ μm. The OT focal plane remains at $z = 6.0$ μm. While the position of the OS focal plane is increased to $z = 12$ μm, the helical phase structure is well maintained. The locations of the OT and OS can even be interchanged with $\Delta f = -3.5$ μm, as shown in Fig. 4(b). Except for the focal lengths, the rotating orbit of the spanner can be tuned as well. Figures 4(c) and 4(d) illustrate an integration of the OT with OS of topological charges $l = 2$ and 3, respectively. However, it is noted that the local intensity of the OS will decrease with increasing l.

In summary, we have demonstrated the possibility of assembling the OTs and OS onto one identical single-layer metasurface. The mechanism is the coexisting geometric and dynamic phases, which confer two kinds of polarization-dependent

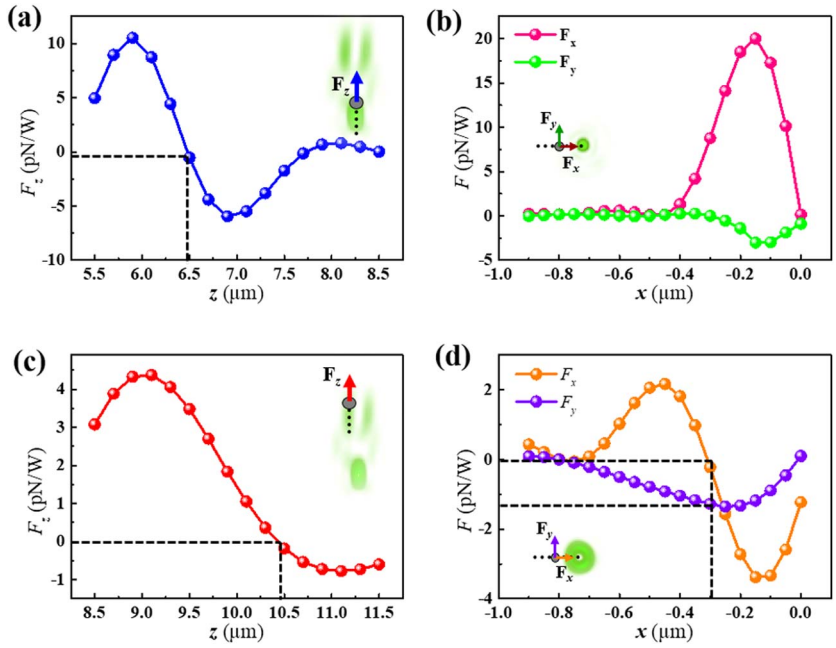

Fig. 3. Calculated optical forces on a PS particle located in the vicinity of (a), (c) the focusing spot and (b), (d) the vortex field. Longitudinal force as a function of the z position of the particle moving along (a) $x = 0$ μm and (c) 0.4 μm. Transverse forces versus the x position of the particle at (b) $z = 6.5$ μm and (d) 10.4 μm.

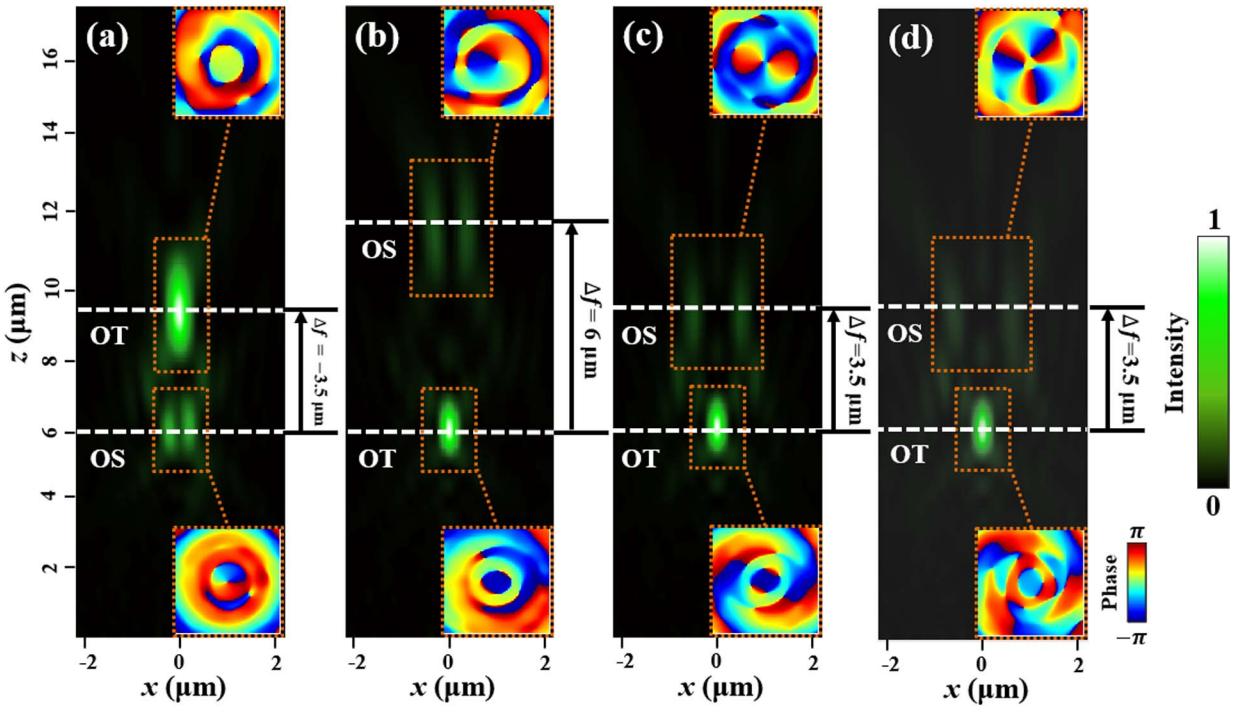

Fig. 4. Simulated field distributions for (a) $\Delta f = -3.5$ μm and $l = 1$; (b) $\Delta f = 6$ μm and $l = 1$; (c) $\Delta f = 3.5$ μm and $l = 2$; (d) $\Delta f = 3.5$ μm and $l = 3$. Insets show the phase profiles at the focal planes indicated by dashed lines.

optical responses upon the metasurface. In addition, since the two optical responses are independent of each other, the focal planes of the tweezers and spanner are adjustable, and the orbit of the spanner can be flexibly tailored. With the merits of miniaturization, integration, and tunability, the dual phase-controlled metasurface is expected to serve in the next generation of optical manipulation devices. We also anticipate that the emerging field of the metasurface could inspire new ideas for achieving exotic optical forces [51–55].

APPENDIX A: DERIVATION OF THE JONES MATRIX $J(X, Y)$ AND ITS EIGENVALUES AND EIGENVECTORS

As we discussed in Section 2, the metasurface with both dynamic and geometric phases is able to achieve two independent optical responses. The following form can be obtained by simplifying Eq. (2):

$$J(x,y) = \frac{1}{2}\begin{bmatrix} e^{i\phi^+(x,y)} + e^{i\phi^-(x,y)} & ie^{i\phi^-(x,y)} - e^{i\phi^+(x,y)} \\ ie^{i\phi^-(x,y)} - ie^{i\phi^+(x,y)} & -ie^{i\phi^+(x,y)} - e^{i\phi^-(x,y)} \end{bmatrix}. \tag{A1}$$

By solving the characteristic equations of Jones matrix $J(x,y)$ in Eq. (A1), we can obtain the eigenvalues

$$\zeta_1 = e^{i\{\frac{1}{2}[\phi^+(x,y)+\phi^-(x,y)]\}},$$
$$\zeta_2 = e^{i\{\frac{1}{2}[\phi^+(x,y)+\phi^-(x,y)]-\pi\}}, \tag{A2}$$

and the eigenvectors

$$|\lambda_1\rangle = \begin{bmatrix} \cos\frac{1}{4}[\phi^+(x,y) - \phi^-(x,y)] \\ \sin\frac{1}{4}[\phi^+(x,y) - \phi^-(x,y)] \end{bmatrix},$$
$$|\lambda_2\rangle = \begin{bmatrix} -\sin\frac{1}{4}[\phi^+(x,y) - \phi^-(x,y)] \\ \cos\frac{1}{4}[\phi^+(x,y) - \phi^-(x,y)] \end{bmatrix}. \tag{A3}$$

Therefore, the Jones matrix $J(x,y)$ can be decomposed into canonical form $J(x,y) = P\Lambda P^{-1}$, where Λ is a diagonal matrix, and P is an invertible matrix. We can write the Jones matrix for the realization of two optical responses as

$$\begin{aligned} J(x,y) &= P\Lambda P^{-1} \\ &= \begin{bmatrix} \cos\frac{1}{4}[\phi^+(x,y) - \phi^-(x,y)] & -\sin\frac{1}{4}[\phi^+(x,y) - \phi^-(x,y)] \\ \sin\frac{1}{4}[\phi^+(x,y) - \phi^-(x,y)] & \cos\frac{1}{4}[\phi^+(x,y) - \phi^-(x,y)] \end{bmatrix} \\ &\times \begin{bmatrix} e^{i\{\frac{1}{2}[\phi^+(x,y)+\phi^-(x,y)]\}} & 0 \\ 0 & e^{i\{\frac{1}{2}[\phi^+(x,y)+\phi^-(x,y)]-\pi\}} \end{bmatrix} \\ &\times \begin{bmatrix} \cos\frac{1}{4}[\phi^+(x,y) - \phi^-(x,y)] & \sin\frac{1}{4}[\phi^+(x,y) - \phi^-(x,y)] \\ -\sin\frac{1}{4}[\phi^+(x,y) - \phi^-(x,y)] & \cos\frac{1}{4}[\phi^+(x,y) - \phi^-(x,y)] \end{bmatrix}. \end{aligned} \tag{A4}$$

Because P can be considered as the rotation matrix of Λ, the phase shift ϕ_x and ϕ_y along two symmetry axes and the rotation angle θ can be written as the following expression:

$$\phi_x = \frac{1}{2}[\phi^+(x,y) + \phi^-(x,y)],$$
$$\phi_y = \frac{1}{2}[\phi^+(x,y) + \phi^-(x,y) - \pi],$$
$$\theta = \frac{1}{4}[\phi^+(x,y) - \phi^-(x,y)]. \quad \textbf{(A5)}$$

Equations (4) and (5) can be obtained by further simplifying Eq. (A5), and therefore we can select the suitable nanobricks and acquire the appropriate orientation angle at each position of the metasurface.

APPENDIX B: PARAMETERS OF SELECTED NANOBRICKS

According to the calculation, the transmittances (T_x and T_y) and phase shifts (ϕ_x and ϕ_y) as a function of the nanobrick size parameters, L and W, covering 50–400 nm, are perfomed by the FDTD method, as shown in Fig. 5, and the 12 selected nanobricks have already been labeled as well as the details being given in Table 1.

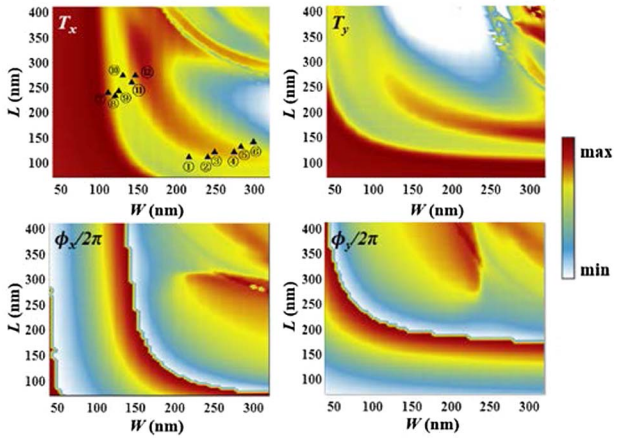

Fig. 5. Transmittances (T_x and T_y) and phase shifts (ϕ_x and ϕ_y) as a function of the nanobrick size parameters, L and W, and the selected nanobricks have already been labeled.

Table 1. Detailed Parameters of the Selected Nanobricks Including Length L, Width W, and Phase Shifts ϕ_x, ϕ_y

L (nm)	W (nm)	ϕ_x ($\phi/2\pi$)	ϕ_y ($\phi/2\pi$)
220	115	0.09	0.61
245	115	0.17	0.64
250	125	0.25	0.78
275	125	0.35	0.80
280	135	0.42	0.89
300	140	0.50	0.97
110	240	0.59	0.12
120	235	0.69	0.17
125	245	0.78	0.23
130	275	0.84	0.38
140	260	0.94	0.38
145	275	0.99	0.47

Funding. National Natural Science Foundation of China (11621091, 11674166, 11674167, 11674168, 11774162, 11774164, 11804119, 11822406, 11834007, 91850204); Key Technologies Research and Development Program (2016YFA0202103, 2017YFA0303700, 2017YFA0303702).

Acknowledgment. The authors are grateful for the stimulating discussions with Professor Shaohui Yan (XIOPM).

Disclosures. The authors declare no conflicts of interest.

REFERENCES

1. A. Ashkin, J. M. Dziedzic, J. E. Bjorkholm, and S. Chu, "Observation of a single-beam gradient force optical trap for dielectric particles," Opt. Lett. **11**, 288–290 (1986).
2. D. G. Grier, "A revolution in optical manipulation," Nature **424**, 810–816 (2003).
3. P. C. Chaumet and M. Nieto-Vesperinas, "Time-averaged total force on a dipolar sphere in an electromagnetic field," Opt. Lett. **25**, 1065–1067 (2000).
4. M. Nieto-Vesperinas, J. J. Saenz, R. Gomez-Medina, and L. Chantada, "Optical forces on small magnetodielectric particles," Opt. Express **18**, 11428–11443 (2010).
5. A. Ashkin, "Acceleration and trapping of particles by radiation pressure," Phys. Rev. Lett. **24**, 156–159 (1970).
6. J. L. Killian, F. Ye, and M. D. Wang, "Optical tweezers: a force to be reckoned with," Cell **175**, 1445–1448 (2018).
7. F. Tebbenjohanns, M. Frimmer, V. Jain, D. Windey, and L. Novotny, "Motional sideband asymmetry of a nanoparticle optically levitated in free space," Phys. Rev. Lett. **124**, 013603 (2020).
8. F. Tebbenjohanns, M. Frimmer, A. Militaru, V. Jain, and L. Novotny, "Cold damping of an optically levitated nanoparticle to microkelvin temperatures," Phys. Rev. Lett. **122**, 223601 (2019).
9. Y. Roichman, B. Sun, A. Stolarski, and D. G. Grier, "Influence of nonconservative optical forces on the dynamics of optically trapped colloidal spheres: the fountain of probability," Phys. Rev. Lett. **101**, 128301 (2008).
10. X. Xu, M. Nieto-Vesperinas, C. W. Qiu, X. Liu, D. Gao, Y. Zhang, and B. Li, "Kerker-type intensity-gradient force of light," Laser Photon. Rev **14**, 1900265 (2020).
11. H. Li, Y. Cao, L.-M. Zhou, X. Xu, T. Zhu, Y. Shi, C.-W. Qiu, and W. Ding, "Optical pulling forces and their applications," Adv. Opt. Photon. **12**, 288–366 (2020).
12. Y. Liang, S. Yan, Z. Wang, R. Li, Y. Cai, M. He, B. Yao, and M. Lei, "Simultaneous optical trapping and imaging in the axial plane: a review of current progress," Rep. Prog. Phys. **83**, 032401 (2020).
13. A. M. Yao and M. J. Padgett, "Orbital angular momentum: origins, behavior and applications," Adv. Opt. Photon. **3**, 161–204 (2011).
14. M. J. Padgett, "Orbital angular momentum 25 years on [invited]," Opt. Express **25**, 11265–11274 (2017).
15. M. Nieto-Vesperinas, "Optical torque: electromagnetic spin and orbital-angular-momentum conservation laws and their significance," Phys. Rev. A **92**, 043843 (2015).
16. S. Yan, M. Li, and B. Yao, "Separation of optical angular momentum flux," J. Opt. **21**, 035606 (2019).
17. N. B. Simpson, K. Dholakia, L. Allen, and M. J. Padgett, "Mechanical equivalence of spin and orbital angular momentum of light an optical spanner," Opt. Lett. **22**, 52–54 (1997).
18. L. Chen, G. Zheng, and W. She, "Electrically and magnetically controlled optical spanner based on the transfer of spin angular momentum of light in an optically active medium," Phys. Rev. A **75**, 061403 (2007).
19. Y. Zhang, W. Shi, Z. Shen, Z. Man, C. Min, J. Shen, S. Zhu, H. P. Urbach, and X. Yuan, "A plasmonic spanner for metal particle manipulation," Sci. Rep. **5**, 15446 (2015).
20. S. Mei, K. Huang, T. Zhang, M. Q. Mehmood, H. Liu, C. T. Lim, J. Teng, and C.-W. Qiu, "Evanescent vortex: optical subwavelength spanner," Appl. Phys. Lett. **109**, 191107 (2016).

21. M. Nieto-Vesperinas, "Optical torque on small bi-isotropic particles," Opt. Lett. **40**, 3021–3024 (2015).
22. M. Dienerowitz, M. Mazilu, P. J. Reece, T. F. Krauss, and K. Dholakia, "Optical vortex trap for resonant confinement of metal nanoparticles," Opt. Express **16**, 4991–4999 (2008).
23. J. R. Arias-Gonzalez and M. Nieto-Vesperinas, "Optical forces on small particles: attractive and repulsive nature and plasmon-resonance conditions," J. Opt. Soc. Am. A **20**, 1201–1209 (2003).
24. A. Arbabi, Y. Horie, M. Bagheri, and A. Faraon, "Dielectric metasurfaces for complete control of phase and polarization with subwavelength spatial resolution and high transmission," Nat. Nanotechnol. **10**, 937–943 (2015).
25. Y. Bao, J. Ni, and C. W. Qiu, "A minimalist single-layer metasurface for arbitrary and full control of vector vortex beams," Adv. Mater. **32**, 1905659 (2020).
26. N. Yu, P. Genevet, M. A. Kats, F. Aieta, J.-P. Tetienne, F. Capasso, and Z. Gaburro, "Light propagation with phase discontinuities generalized laws of reflection and refraction," Science **334**, 333–337 (2011).
27. L. Huang, X. Chen, H. Muhlenbernd, G. Li, B. Bai, Q. Tan, G. Jin, T. Zentgraf, and S. Zhang, "Dispersionless phase discontinuities for controlling light propagation," Nano Lett. **12**, 5750–5755 (2012).
28. S. Wang, P. C. Wu, V. C. Su, Y. C. Lai, C. Hung Chu, J. W. Chen, S. H. Lu, J. Chen, B. Xu, C. H. Kuan, T. Li, S. Zhu, and D. P. Tsai, "Broadband achromatic optical metasurface devices," Nat. Commun. **8**, 187 (2017).
29. W. T. Chen, A. Y. Zhu, V. Sanjeev, M. Khorasaninejad, Z. Shi, E. Lee, and F. Capasso, "A broadband achromatic metalens for focusing and imaging in the visible," Nat. Nanotechnol. **13**, 220–226 (2018).
30. S. Wang, P. C. Wu, V. C. Su, Y. C. Lai, M. K. Chen, H. Y. Kuo, B. H. Chen, Y. H. Chen, T. T. Huang, J. H. Wang, R. M. Lin, C. H. Kuan, T. Li, Z. Wang, S. Zhu, and D. P. Tsai, "A broadband achromatic metalens in the visible," Nat. Nanotechnol. **13**, 227–232 (2018).
31. R. J. Lin, V. C. Su, S. Wang, M. K. Chen, T. L. Chung, Y. H. Chen, H. Y. Kuo, J. W. Chen, J. Chen, Y. T. Huang, J. H. Wang, C. H. Chu, P. C. Wu, T. Li, Z. Wang, S. Zhu, and D. P. Tsai, "Achromatic metalens array for full-colour light-field imaging," Nat. Nanotechnol. **14**, 227–231 (2019).
32. L. Li, Z. Liu, X. Ren, S. Wang, V.-C. Su, M.-K. Chen, C. Chu, K. H. Yu, B. Liu, W. Zang, G. Guo, L. Zhang, Z. Wang, S. Zhu, and D. P. Tsai, "Metalens-array–based high-dimensional and multiphoton quantum source," Science **368**, 1487–1490 (2020).
33. T. Li, X. Li, S. Yan, X. Xu, S. Wang, B. Yao, Z. Wang, and S. Zhu, "Generation and conversion dynamics of dual Bessel beams with a photonic spin-dependent dielectric metasurface," Phys. Rev. Appl. **15**, 014059 (2021).
34. E. Nazemosadat, M. Mazur, S. Kruk, I. Kravchenko, J. Carpenter, J. Schröder, P. A. Andrekson, M. Karlsson, and Y. Kivshar, "Dielectric broadband metasurfaces for fiber mode-multiplexed communications," Adv. Opt. Mater. **7**, 1801679 (2019).
35. S. Li, X. Li, G. Wang, S. Liu, L. Zhang, C. Zeng, L. Wang, Q. Sun, W. Zhao, and W. Zhang, "Multidimensional manipulation of photonic spin Hall effect with a single-layer dielectric metasurface," Adv. Opt. Mater. **7**, 1801365 (2018).
36. S. Li, X. Li, L. Zhang, G. Wang, L. Zhang, M. Liu, C. Zeng, L. Wang, Q. Sun, W. Zhao, and W. Zhang, "Efficient optical angular momentum manipulation for compact multiplexing and demultiplexing using a dielectric metasurface," Adv. Opt. Mater. **8**, 1901666 (2020).
37. J. P. Balthasar Mueller, N. A. Rubin, R. C. Devlin, B. Groever, and F. Capasso, "Metasurface polarization optics: independent phase control of arbitrary orthogonal states of polarization," Phys. Rev. Lett. **118**, 113901 (2017).
38. W. Cai, H. Yu, S. Xu, M. Xia, T. Li, Y. Yin, Y. Xia, and J. Yin, "Optical focusing based on the planar metasurface reflector with application to trapping cold molecules," J. Opt. Soc. Am. B **35**, 3049–3054 (2018).
39. T. Chantakit, C. Schlickriede, B. Sain, F. Meyer, T. Weiss, N. Chattham, and T. Zentgraf, "All-dielectric silicon metalens for two-dimensional particle manipulation in optical tweezers," Photon. Res. **8**, 1435–1440 (2020).
40. L. Ma, J. Guan, Y. Wang, C. Chen, J. Zhang, J. Lin, J. Tan, and P. Jin, "Diffraction-limited axial double foci and optical traps generated by optimization-free planar lens," Nanophotonics **9**, 841–853 (2020).
41. A. Eremin, P. Hirankittiwong, N. Chattham, H. Nadasi, R. Stannarius, J. Limtrakul, O. Haba, K. Yonetake, and H. Takezoe, "Optically driven translational and rotational motions of microrod particles in a nematic liquid crystal," Proc. Natl. Acad. Sci. USA **112**, 1716–1720 (2015).
42. H. Sroor, Y.-W. Huang, B. Sephton, D. Naidoo, A. Vallés, V. Ginis, C.-W. Qiu, A. Ambrosio, F. Capasso, and A. Forbes, "High-purity orbital angular momentum states from a visible metasurface laser," Nat. Photonics **14**, 498–503 (2020).
43. S. Suwannasopon, F. Meyer, C. Schlickriede, P. Chaisakul, J. Thienprasert, J. Limtrakul, T. Zentgraf, and N. Chattham, "Miniaturized metalens based optical tweezers on liquid crystal droplets for lab-on-a-chip optical motors," Crystals **9**, 515 (2019).
44. S. Yan, M. Li, Y. Liang, Y. Cai, and B. Yao, "Spin momentum-dependent orbital motion," New J. Phys. **22**, 053009 (2020).
45. X. Xu, C. Cheng, H. Xin, H. Lei, and B. Li, "Controllable orientation of single silver nanowire using two fiber probes," Sci. Rep. **4**, 3989 (2014).
46. J. D. Jackson, *Classical Electrodynamics*, 3rd ed. (Wiley, 1998).
47. A. Rohrbach, "Stiffness of optical traps: quantitative agreement between experiment and electromagnetic theory," Phys. Rev. Lett. **95**, 168102 (2005).
48. M. V. Berry, "Optical currents," J. Opt. A **11**, 094001 (2009).
49. A. Y. Bekshaev and M. S. Soskin, "Transverse energy flows in vectorial fields of paraxial beams with singularities," Opt. Commun. **271**, 332–348 (2007).
50. A. Bekshaev, K. Y. Bliokh, and M. Soskin, "Internal flows and energy circulation in light beams," J. Opt. **13**, 053001 (2011).
51. X. Xu, C. Cheng, Y. Zhang, H. Lei, and B. Li, "Scattering and extinction torques: how plasmon resonances affect the orientation behavior of a nanorod in linearly polarized light," J. Phys. Chem. Lett. **7**, 314–319 (2016).
52. H. Li, Y. Cao, B. Shi, T. Zhu, Y. Geng, R. Feng, L. Wang, F. Sun, Y. Shi, M. A. Miri, M. Nieto-Vesperinas, C. W. Qiu, and W. Ding, "Momentum-topology-induced optical pulling force," Phys. Rev. Lett. **124**, 143901 (2020).
53. T. Zhu, Y. Shi, W. Ding, D. P. Tsai, T. Cao, A. Q. Liu, M. Nieto-Vesperinas, J. J. Saenz, P. C. Wu, and C. W. Qiu, "Extraordinary multipole modes and ultra-enhanced optical lateral force by chirality," Phys. Rev. Lett. **125**, 043901 (2020).
54. H. Chen, H. Zheng, W. Lu, S. Liu, J. Ng, and Z. Lin, "Lateral optical force due to the breaking of electric-magnetic symmetry," Phys. Rev. Lett. **125**, 073901 (2020).
55. X. Xu and M. Nieto-Vesperinas, "Azimuthal imaginary Poynting momentum density," Phys. Rev. Lett. **123**, 233902 (2019).